npj | clean water

Article

Published in partnership with King Fahd University of Petroleum & Minerals

https://doi.org/10.1038/s41545-025-00526-7

Scalable brine treatment using 3D-printed multichannel thermodiffusion

Milad Mohsenzadeh[1,3], Shuqi Xu[1,2,3], Osman Shamet[1] & Juan F. Torres[1,2] ✉

Industrial processes generate over 200 million metric tonnes of brine each day, posing serious environmental challenges due to its high salinity, toxicity, and energy-intensive treatment requirements. Conventional treatment methods, such as reverse osmosis and evaporation ponds, face limitations in scalability, energy efficiency, and environmental impact. Here, we demonstrate that *multichannel thermodiffusion*—an emerging membrane- and evaporation-free method driven by temperature gradients—can effectively concentrate brines beyond 70 ppt (parts per thousand), approaching saturation. Using a liquid Burgers cascade, we show that thermodiffusive separation becomes more efficient at higher feed concentrations and can be scaled using low-cost, rapidly fabricated 3D-printed components. Furthermore, we demonstrate the versatility of the technique by applying it to an industrially relevant feed including LiI, K_2SO_4, and NaOH. Our results indicate that thermodiffusion, previously regarded as 'too weak for practical use', offers a sustainable, scalable, and energy-efficient pathway toward minimal liquid discharge and potentially resource recovery from concentrates.

Brine, an environmentally hazardous solution with salinity exceeding seawater, is produced at 200 million tonnes daily. Brine is discharged from various industrial processes, including desalination, pharmaceuticals, petrochemicals, textiles, dairy, and oil & gas (O&G) extraction. The common concentration range is between 50 ppt (parts per thousand) and 150 ppt, but can be as high as 400 ppt from O&G produced water. However, the adverse environmental impact of the discharged brine is substantial, including the destruction of marine ecosystems and the pollution of precious groundwater resources[1,2]. The main challenge in brine treatment is that the existing technologies based on functional materials, such as reverse osmosis membranes, are limited to about 70 ppt with low recovery rates (as low as 10%)[3]. Furthermore, conventional thermal methods for brine concentration, such as evaporation ponds, are too slow, susceptible to weather variability, and require a large land area[4]. Critically, they lead to the depletion of water resources in arid and semi-arid regions because water is lost to the atmosphere during evaporation. More modern techniques that include water recovery, such as multiple effect distillation (MED), may suffer from severe scaling[5]. In addition, new crystallisation technologies, such as membraneless solvent-based methods[6], are promising, but have high capital and operating costs and struggle with complete solvent removal. Currently, there is no sustainable scalable technology for brine treatment.

Brine typically contains ions of sodium, chloride, calcium and potassium at high concentrations, and salt harvesting can be economically profitable[3]. Importantly, high-value metals—such as lithium, rubidium, and caesium—can be found in brine[7]. In fact, brine treatment is an integral part of the extraction of these raw materials essential for infrastructure, manufacturing, and energy production. However, as with most mining practices, there are concerns about the use of land, energy and water, leading to an increasing demand for sustainable technologies. Furthermore, there are potentials in new areas for recovery of valuable materials from brines and other concentrates. For example, potash is a valuable fertiliser obtained from evaporation[8]. Currently, over 80% of brine is directly disposed of by surface discharge, wastewater discharge, or deep-well injection. This not only raises environmental concerns[9], but also means missed opportunities to recover water and critical resources[3]. An emerging trend in brine treatment is to maximise freshwater recovery and minimise waste disposal, namely minimal liquid discharge (MLD, in which ≥95% of water is harvested) and zero liquid discharge (ZLD, 100% of water is harvested). The typical method used here is evaporation ponds, which are also used in brine mining to increase the concentration of lithium and potash from the initial, more dilute concentrations. However, this method is excessively time consuming (6–24 months) and occupies vast land area. The challenges intrinsic to existing brine treatment technologies, along with the opportunities associated with brine mining, highlight the urgent need to develop new low-cost and sustainable concentration technologies for brines and other concentrates.

This could be enabled by thermodiffusion or the Soret effect[10], a phenomenon characterised by mass transport under a temperature gradient[11]. We showed the potential of thermodiffusion for high-throughput

[1]ANU HEAT Lab, School of Engineering, The Australian National University, Canberra, ACT, Australia. [2]Soret Technologies, Canberra, ACT, Australia. [3]These authors contributed equally: Milad Mohsenzadeh, Shuqi Xu. ✉e-mail: felipe.torres@anu.edu.au

applications of desalination and brine concentration[10,12]. Although the Soret effect is generally a weak phenomenon, our innovation in multichannel thermodiffusion (MTD) with hardware improvements (u-shaped heating near the channel walls and selective thermal insulation through the liquid Burgers cascade) increased performance, up to 40 times compared to a baseline case without improvements. Importantly, we experimentally showed that the thermodiffusive separation at salinities of 70 ppt is greater than that of 35 ppt. A better energy efficiency at higher concentrations, up to saturation, can be achieved because the thermodiffusive flux becomes stronger. The total mass flux under temperature gradients is

$$\mathbf{J} = -\rho D\nabla C - \rho C(1-C)D_{\mathrm{T}}\nabla T, \quad (1)$$

where the first term on the right-hand side of the equation describes Fickian mass diffusion (due to the concentration gradient ∇C) and the second term describes thermodiffusion (due to a temperature gradient ∇T). In Eq. (1), D is the Fickian diffusion coefficient, which is always positive because net diffusive transport spontaneously occurs from high to low concentration due to Brownian motion. In contrast, D_{T} is the thermodiffusion coefficient that can be positive (thermophobic) or negative (thermophilic), depending on the system[13]. Seawater is a multi-component aqueous solution, but a quasi-binary approximation could be relatively accurate due to electroneutrality[14]. The Soret coefficient S_{T} is defined as the ratio between the thermodiffusion and Fickian diffusion coefficients $S_{\mathrm{T}} \equiv D_{\mathrm{T}}/D$, and indicates the level of separation in steady state under both Fickian and thermodiffusive mass fluxes.

In this study, our aim is to address the following research questions that enable the adoption of thermodiffusive brine concentration technology.

1. *Can MTD be used to concentrate brine beyond 70 ppt to close to saturation levels?* It was suggested in refs. 10,12 without experimental evidence.
2. *Can MTD structures be manufactured with low-cost scalable methods?* Computer numerical control (CNC) machining was previously used[10], but it is expensive and not suitable for rapid prototyping or mass production.
3. *Can multichannel arrangements have different shapes that are not a long straight array of channels?* A practical liquid Burgers cascade may need lengths exceeding 10 m, which are not practical. Serpentine structures would facilitate the scalability.
4. *How does thermodiffusive separation perform for different types of brines important in the mining industry?* in refs. 10,12, the technology was demonstrated with seawater and NaCl brines. Expanding this application to other types of brine would greatly expand its field of application.

In this work, we provide the first experimental evidence that thermodiffusive separation is more effective at higher feed concentrations, and this trend persists even near saturation. The ability of MTD to handle such highly concentrated feeds, in contrast to membrane-based technologies, highlights its potential for brine treatment. Furthermore, based on an ongoing techno-economic analysis (TEA)[15], we identified that reducing manufacturing costs is essential for MTD to become economically viable. To this end, we experimentally demonstrate that low-cost, 3D printing-based manufacturing can be used to fabricate the multichannel structure, supporting rapid prototyping and potential widespread adoption. In addition, we predict the performance of MTD for various types of brines in full-scale devices through modelling and provide the corresponding specific energy consumption SEC, i.e., the energy consumption per unit volume of yield.

Results

Liquid Burgers cascade for multichannel thermodiffusive separation

The liquid Burgers cascade (LBC) is a network of thermodiffusive microseparators or channels[16], as shown in Fig. 1a, which enhance the inherently weak thermodiffusive separation in individual channels. Each channel has a flow of momentum, heat and species, as shown in Fig. 1b. A vertical temperature gradient is imposed across each channel, with the upper wall heated and the lower wall cooled to avoid natural convection. This temperature difference drives solute transport via the Soret effect, creating a vertical concentration profile. For thermophobic transport, high concentration develops near the cooled lower wall, while low concentration develops near the heated upper wall. The hydrodynamic and thermal entrance lengths are less than 1% of the total channel length. Thus, the flow in the thermodiffusive separation channel is a laminar, fully-developed planar Poiseuille flow with a positive quasi-linear temperature profile. The mass transport is advection-dominant along the channel (Péclet number $\mathrm{Pe}_x \gg 1$) while diffusion and thermodiffusion dominate across the channel height ($\mathrm{Pe}_y = 0$). These ideal assumptions were considered in the experimental design and experimentally validated in our previous work (Figs. 2 and 3 of ref. 17, Supplementary Method 2 and Fig. 2 of ref. 12). The LBC requires a fully developed laminar flow to maintain stratification, as vertical laminar flows or turbulence would mix the species, reducing or suppressing the species separation achieved by thermodiffusion.

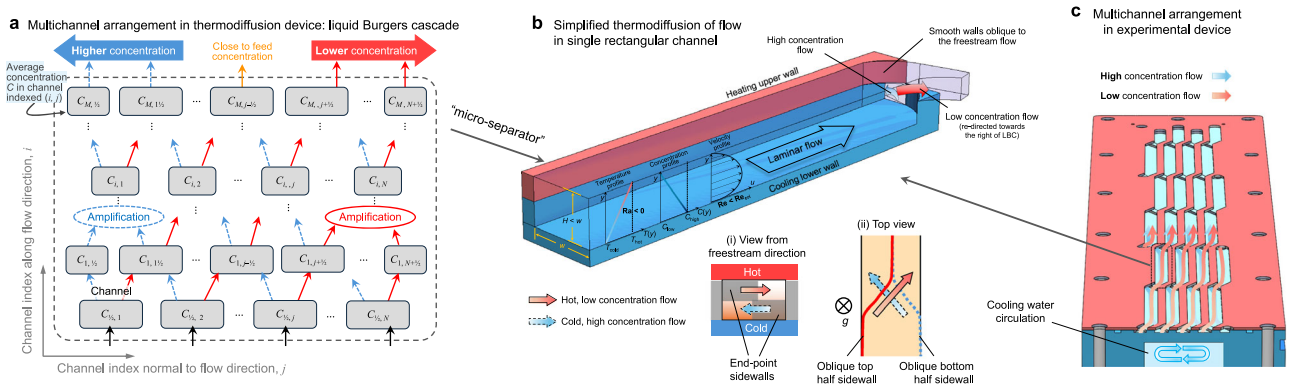

Fig. 1 | The concept of multichannel thermodiffusion (MTD). a Schematic showing the arrangement of flow within the MTD device called the liquid Burger cascade (LBC), illustrates how the concentration of a solution separates into higher and lower values on opposite sides of the device, perpendicular to the main flow direction. **b** Illustration of a single rectangular channel within the LBC. A laminar Poiseuille plane flow (Reynolds number below a critical threshold, $\mathrm{Re} < \mathrm{Re}_{\mathrm{cri}}$) with a parabolic horizontal velocity $v(y)$ passes through a rectangular channel while having a positive vertical temperature gradient. In the x direction, the Péclet number $\mathrm{Pe} \gg 1$ so that advective mass transport is dominant. In the y direction, $\mathrm{Pe} = 0$ and the mass transport is diffusion dominant. The flow bifurcates into two at the channel outlet. If the solute is thermophobic, the inset shows that the low concentration flow at the top is deviated towards the right, while the high concentration flow at the bottom is directed towards the left. **c** Flow in the experimental LBC device used in this work.

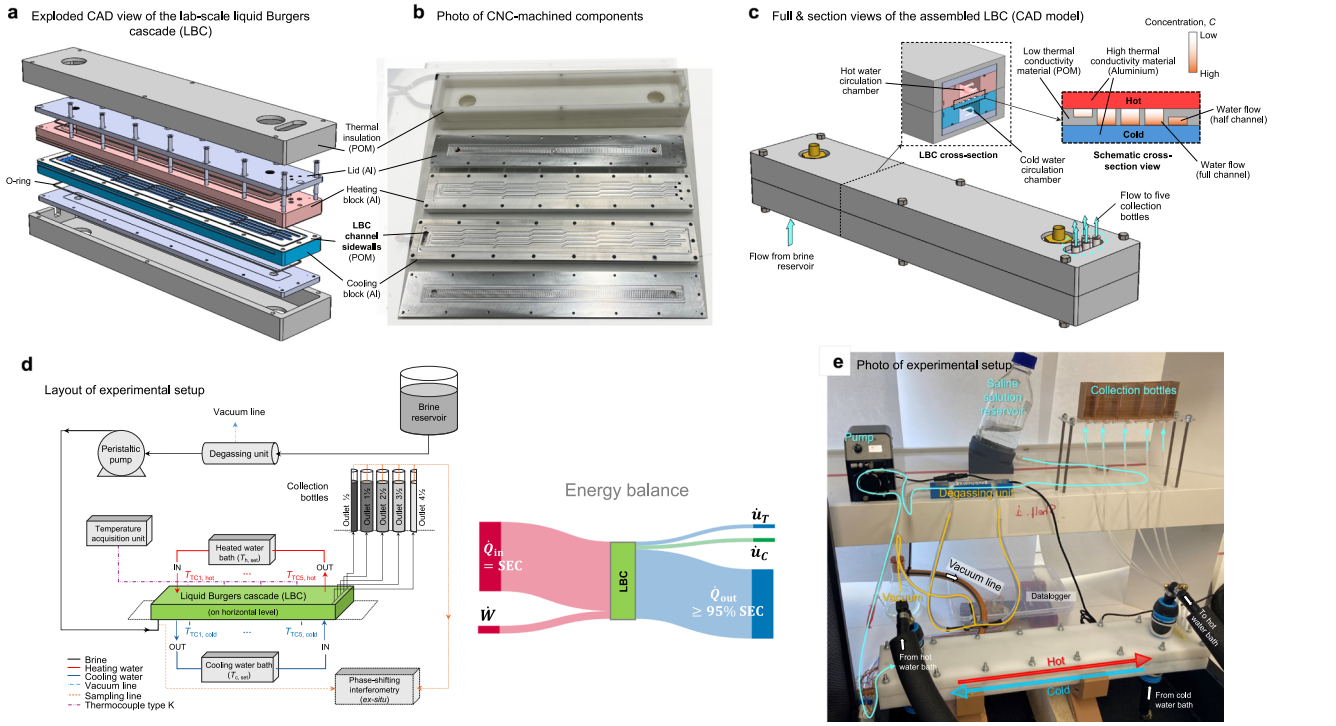

Fig. 2 | The experimental setup for testing the liquid Burgers cascade (LBC). **a** Exploded CAD view of the lab-scale LBC designed to test brine concentration and desalination, showing the key components of the assembly in exploded view. **b** Photo of CNC-machined components. **c** CAD view of the assembled LBC with a cross-sectional view illustrating the arrangement of adjacent channels and their interaction with flow and heating/cooling media. The arrangement of the materials with different thermal conductivities improves thermal energy utilisation. **d** Flow diagram of the experimental setup developed in this study, including instruments and components connected to the LBC. The energy flow in a steady state condition is shown in a Sankey diagram, also described in the Methods section. More than 99% of the energy input to the LBC is the heat transfer rate $\dot{Q}_{in} \approx$ SEC. No heat recovery of $\dot{Q}_{out}$ is considered. **e** Photo of the complete experimental setup.

In the cascade, at the outlet of each channel, the top stream and the bottom stream smoothly bifurcate at the horizontal midplane and no mixing occurs (inset of Fig. 1b). The bottom stream proceeds to the left, while the top stream proceeds to the right. Every channel within the LBC receives two dissimilar inlet streams from adjacent channels of the previous row (except for the channels in the first row and the outer-most columns). Across multiple channels, the channels on the left side progressively accumulate higher concentration streams, while those on the right become increasingly diluted (assuming thermophobic behaviour; the opposite would occur for thermophilic transport). This iterative splitting amplifies the weak thermodiffusive separation in a single channel, increasing the concentration difference between the leftmost and rightmost channels.

CNC-machined LBC

Figure 1c shows the experimental LBC setup, where the multichannel array is clamped between thermostatically controlled plates. To experimentally validate the concept of MTD, a precision CNC-machined LBC was constructed as shown in Fig. 2a–c, using aluminium for the upper and lower channel walls and polyoxymethylene (POM) for the channel sidewalls. The LBC assembly comprises 36 interconnected rectangular channels (28 full channels and 8 half channels) arranged in a matrix of 4 × 4 channel pairs. The exploded CAD view (Fig. 2a) illustrates the multilayer assembly, in which each component (thermal insulation shield, aluminium lid, heating block, LBC channels, and cooling block) was machined and vertically stacked to ensure precise alignment and effective sealing. Aluminium walls facilitate thermal regulation and reduce thermal resistance, while POM components provide structural support and reduce parasitic heat losses through the structure, hence improving thermal energy utilisation. Based on a previous thermal resistance network analysis of the same device with sidewalls made of POM and water as the working fluid, $R_{sidewall} = 0.36\,KW^{-1}$ and $R_{fluid} = 0.43\,KW^{-1}$. In that case, approximately 50% of the heat is transferred through the LBC structure and 50% through the solution. A pair of water baths was integrated above and below the channel blocks to circulate hot and cold water to establish a stable vertical temperature difference between the walls. The average temperature difference of 47.5 K was measured via 5 pairs of Type K thermocouples located on the side of heating and cooling blocks, all 5 mm away from the channel upper and lower walls. This configuration follows the LBC arrangement in Fig. 1a, enabling the study of the thermodiffusive separation under controlled laboratory conditions.

The experimental layout is presented in Fig. 2d–e with a schematic and a photo. The unit was positioned horizontally on a level platform to ensure uniform laminar flow across all channels. The feed water from an elevated brine reservoir was degassed before entering the LBC to eliminate the possible generation of air bubbles that affect separation. Control of the volumetric flow rate was achieved through a calibrated peristaltic pump. The total length of the device is approximately 500 mm, while the total length of each channel pair is 115 mm with a single channel length of 56 mm. The flow exits through five outlets, three full channels (1+1/2, 2+1/2 and 3+1/2) and two half channels (1/2 and 4+1/2), each leading to individual collection bottles placed at equal heights. To compensate for the half-height channels at the first and last outlets of the LBC, the corresponding collection bottles were arranged with flow-volume restrictors reducing the cross-sectional area of the collection bottle to half, ensuring synchronised rise levels across all bottles (producing equal hydrostatic pressure at the LBC outlets). After steady-state operation, samples were extracted from each collection bottle to measure the concentration difference between the inlet and outlet streams. Phase-shifting interferometry (PSI)[13,18] provided an accurate quantification of the concentration difference between the outlet samples and the feed water. Monotonic changes in concentration difference are expected along the outlet streams[10] and, in this work, we focus on the application of brine concentration.

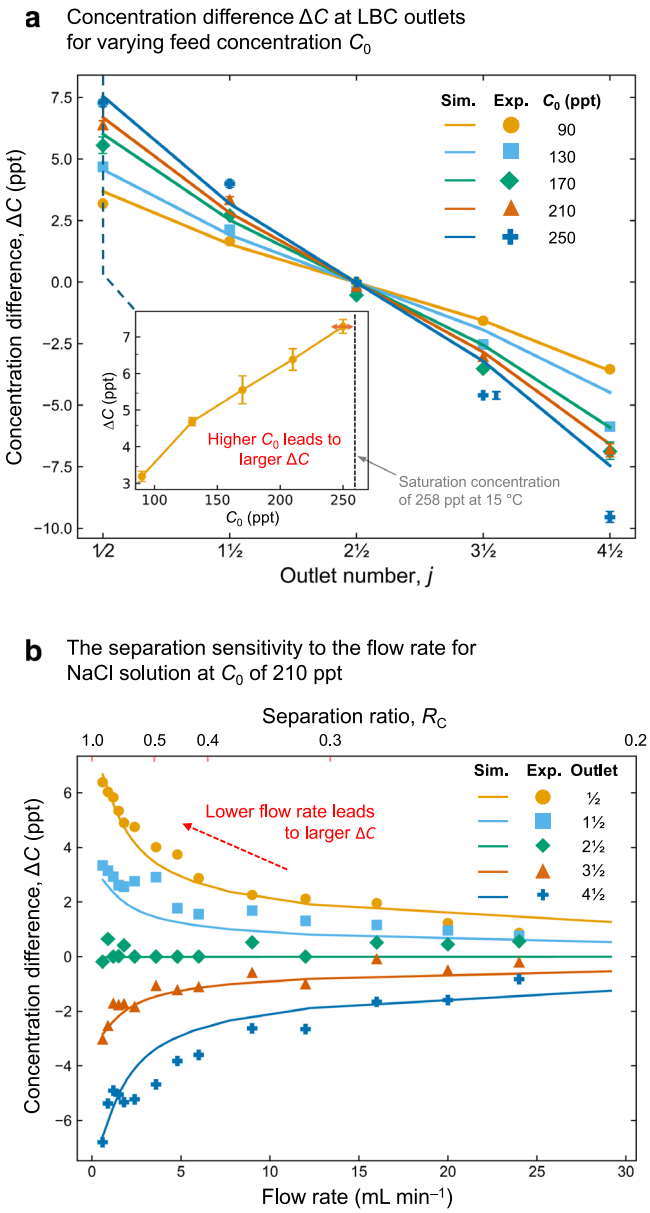

Fig. 3 | Performance of the lab-scale LBC under varying experimental conditions. **a** Concentration difference ΔC between channel outlet and feed with numerical predictions for the NaCl feed concentrations indicated in the legend. The inset plots ΔC at outlet 1/2 as a function of feed concentration C_0. The error bars for PSI measurements represent propagated uncertainties $\delta\Delta C$, derived through error propagation of the standard deviation $\delta\Delta\psi$ of the phase difference $\Delta\psi$ and the standard deviation δCF of the contrast factor. That is, $\delta\Delta C/\Delta C = [(\delta\Delta\psi/\Delta\psi)^2 + (\delta CF/CF)^2]^{0.5}$ (details in Supplementary Method 1 of ref. 10). The inset plots ΔC at outlet 1/2 as a function of feed concentration C_0. The Soret and mass diffusion coefficients are evaluated at the mean temperature of 40 °C to be 2.11×10^{-3} K^{-1} [24] and 2.21×10^{-9} m^2 s^{-1} [34], respectively. Experimental conditions: ΔT = 35 K, Q = 0.6 mL min^{-1}. **b** Concentration difference between the outlet and inlet flows as a function of the volumetric flow rate through the LBC. The flow rate was varied over the range 0.6 mL min^{-1} to 24 mL min^{-1} for a NaCl feed concentration of 210 ppt and ΔT = 35 K. The maximum relative error in these measurements was below 10%. The error bars were omitted in this plot for clarity. The numerical predictions are plotted for comparison.

Separation of species in hypersaline brines

The LBC performance was further investigated in a range of feed concentrations of NaCl to evaluate its suitability to concentrate hypersaline solutions. Figure 3a shows the concentration difference between outlet and inlet streams as a function of outlet number for different feed concentrations. The results show that increasing the feed concentration leads to a greater thermodiffusive separation. Experiments were conducted with inlet salinities ranging from 90 ppt to 270 ppt under a temperature difference of 40 K. The inset of Fig. 3a plots the concentration difference between the first outlet and feed as a function of feed concentration, which clearly shows that a larger separation is achieved as the feed concentration is increased. This is in stark contrast to other brine concentration technologies, such as reverse osmosis (membrane-based method) and air gap membrane distillation (thermal-based) in which a higher concentration leads to performance and materials degradation. Simulations were carried out for each experimental condition following the third step in "Liquid Burgers cascade modelling" in the Methods section to map the concentration in each channel within the LBC, and the numerical results are also plotted. The high degree of agreement between experimental and numerical results confirms that the separation of the high- and low-concentration streams occurred at the horizontal midplane with little mixing, following the horizontal flow depicted in the insets of Fig. 1b. The resulting outlet concentrations demonstrated a nearly linear concentration change from the first to the last outlet, in agreement with the modelling results (previously reported in ref. 10).

These results validate the hypothesis that the thermodiffusive separation amplifies with increased feed concentration up to near-saturation levels as long as the saturation concentration is lower than $C = 0.5$, as described in Eq. (1), a characteristic advantage of MTD involving highly saline waste streams. This enhances the efficiency of the LBC in separating ions at elevated concentrations, making it a promising candidate for integration into ZLD and MLD systems and advanced brine management in desalination plants. The demonstrated ability of the LBC to operate effectively under hypersaline conditions confirms the potential of the system for industrial deployment where conventional methods face efficiency and energy limitations.

Separation sensitivity to LBC flow rate

The performance of the LBC was evaluated across a range of flow rates to understand the effect of throughput on thermodiffusive separation. As shown in Fig. 3b, the outlet concentration profiles were measured for flow rates ranging from 0.6 mL min^{-1} up to 24 mL min^{-1}. The lowest flow rate produced a clear and strong separation effect, with a significant concentration difference between the outlets. This larger separation is attributed to a longer residence time within each channel, which allows thermodiffusion-induced concentration stratification to fully develop. As the flow rate increased, a gradual drop in separation performance occurred, showing a tendency to zero separation. This reduction in separation is due to the decrease in the residence time of the fluid in each channel, quantified by the parameter of the separation ratio R_C, as described in ref. 10. A reduction in R_C (i.e., a partial separation deviating from the fully-developed concentration profile) limits the magnitude of the thermodiffusion-induced concentration difference, but the volumetric flow rate of the process can be increased. If the flow rate is increased beyond the critical Reynolds number, it results in vertical mixing that disrupts the delicate thermodiffusive separation. Interestingly, the separation becomes less sensitive to changes in flow rate after volumetric flow rates of about 5 mL min^{-1} in our setup. Figure 3b reflects this behaviour as a two-stage response as the flow rate is increased: an initial steep decline in the concentration difference followed by a moderate change. Therefore, there is a trade-off in LBC operational flow rate: lower flow rates favour better separation because of a fully developed ion separation, whereas higher flow rates increase system throughput but can reduce the degree of separation. Identifying an optimal flow rate is essential to maximise brine concentration performance without excessively sacrificing yield. More channels in the LBC can compensate for the reduction in concentration difference, reaching optimal values of volumetric flow rate per heat rate (as described in Fig. 4d of ref. 10).

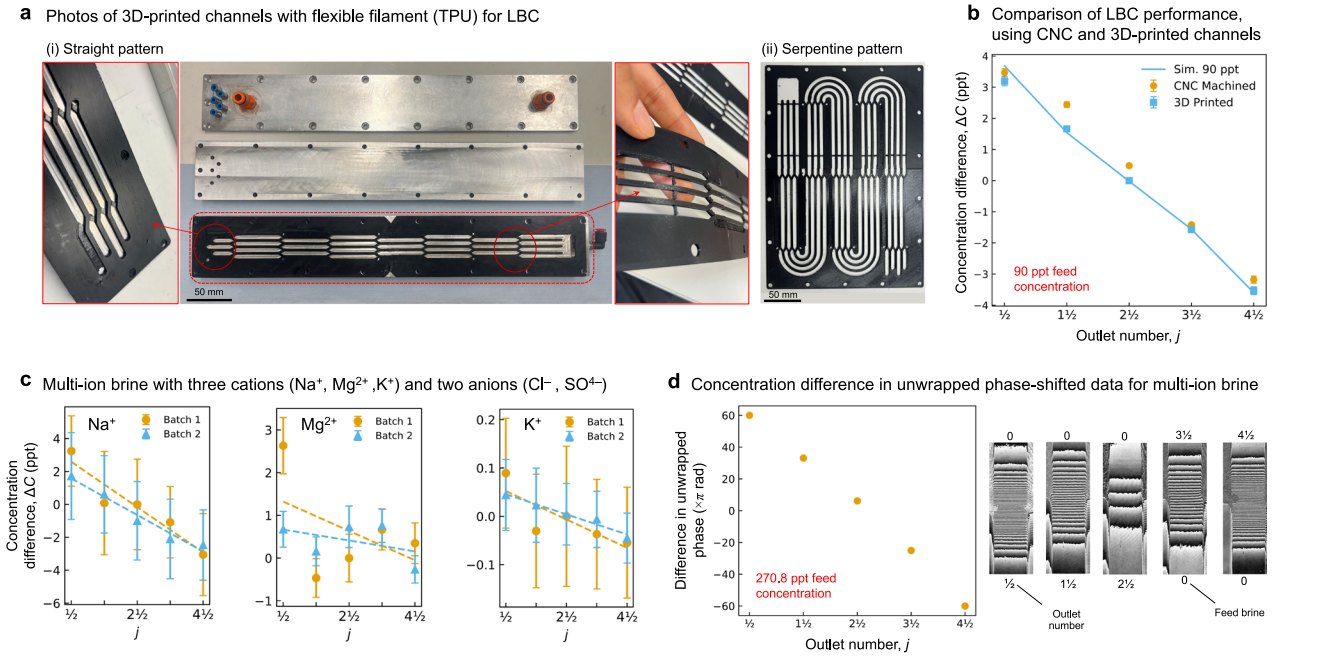

Fig. 4 | 3D-printed LBC channels and multi-ion solutions. a Photo of 3D-printed multichannel inserts fabricated using flexible TPU filament, featuring two flow configurations: (i) straight channel pattern, and (ii) serpentine channel pattern. These were assembled into the lab-scale LBC device. **b** Experimental comparison between data obtained with the CNC-machined channels and 3D-printed channels when NaCl feed concentration is 90 ppt. The other test conditions were identical to Fig. 3a: $\Delta T = 35$ K, and $Q = 0.6$ mL min^{-1}. ΔC was measured with PSI, and the error bars are propagated uncertainties $\delta\Delta C$. **c** A multi-ion solution at a concentration of 270.8 ppt was used as the feed for the 3D-printed LBC. The solution is composed of three cations (Na^+, Mg^{2+}, and K^+) and two anions (Cl^- and SO_4^{2-}), as indicated in the Methods section. Batches 1 and 2 were separately prepared and passed through the LBC. Inductively coupled plasma-mass spectrometry (ICP-MS) was used to measure concentration of each type of cation with five independent measurements for each sample; error bars represent their standard deviation. **d** The phase difference, which is indicative of ΔC, as a function of outlet number for Batch 1. The phase difference is proportional to the collective concentration difference of all the ions between two solutions[10,12].

3D-printed LBC

To explore scalable and low-cost rapid manufacturing methods, a 3D-printed version of the LBC was developed using thermoplastic polyurethane (TPU) and fabricated using fused filament fabrication. As shown in Fig. 4ai, the printed channels successfully replicated the straight-channel arrangement with a flexible material. In addition to this, an alternative serpentine channel configuration was 3D printed and tested within a similar housing unit to investigate geometrical effects on separation performance. The flexible TPU materials for the channel sidewalls had accurate channel dimensions (±0.01 mm) and simplified the assembly of the LBC, indicating a strong advantage in terms of a reliable assembly without cross-channel contamination (since the TPU can be slightly compressed to improve sealing) and facile manufacturing (compared to CNC machining).

Performance testing of the 3D-printed straight channel unit under the same experimental conditions as the CNC prototype revealed a high degree of agreement in the obtained concentration difference, as shown in Fig. 4b. The thermodiffusive separation profiles matched closely, confirming that the thermodiffusive separation process remains effective despite possible minor variations introduced by the 3D-printed structure, such as surface roughness. The results also suggest that sufficient temperature stratification and flow stability were maintained in the printed setup. These findings establish the viability of 3D printing as a rapid prototyping method for LBC design refinement and demonstrate its potential for cost-effective, large-scale manufacturing. The added flexibility in channel design and material choice makes this approach particularly attractive for future development aimed at field deployment and customisable liquid separation applications for a variety of solutions and mixtures. The 3D-printed TPU prototypes were tested under controlled laboratory conditions over several test days to demonstrate proof of concept. During these tests, no measurable performance degradation was observed due to scaling or corrosion. A simple cleaning procedure—flushing the system with deionised water and drying the channel surfaces with airflow—was applied at the end of each test day to maintain short-term operability. We note that long-term durability, fouling behaviour, and chemical resistance in hypersaline and chemically aggressive environments remain critical challenges and will be addressed in future work.

Full-scale LBC with design improvements

An in-house MATLAB code[19], made open-source, was used to model the thermodiffusive separation throughout the LBC including individual channels and to visualise the concentration distribution in the LBC in terms of the average concentration of each channel. The simulation results are shown in Fig. 5a for the lab-scale LBC having 4×4 channel pairs. The table on top of the figure compares the measured experimental values of concentration (same data as in Fig. 3a, which was presented as concentration differences) and the modelled values for a feed concentration of 210 ppt. The excellent agreement between simulation and experimental results validates our in-house modelling tool. This is thus expanded to model full-scale LBCs. The serpentine configuration shown in Fig. 4 and the full-scale LBC analysis presented in this study were designed to demonstrate that the LBC concept can be enlarged without altering its fundamental operational requirements. In principle, larger-scale implementations can achieve modelled performance by proportionally scaling the pumping and heating/cooling units with the device channel area. The current study is based on a system-level energy balance (Fig. 2d) and supported by a separate ongoing techno-economic analysis[15], providing meaningful projections. While this work is limited to lab-scale demonstrations and simulations, these results establish a foundation for assessing integration constraints and operational considerations in future studies.

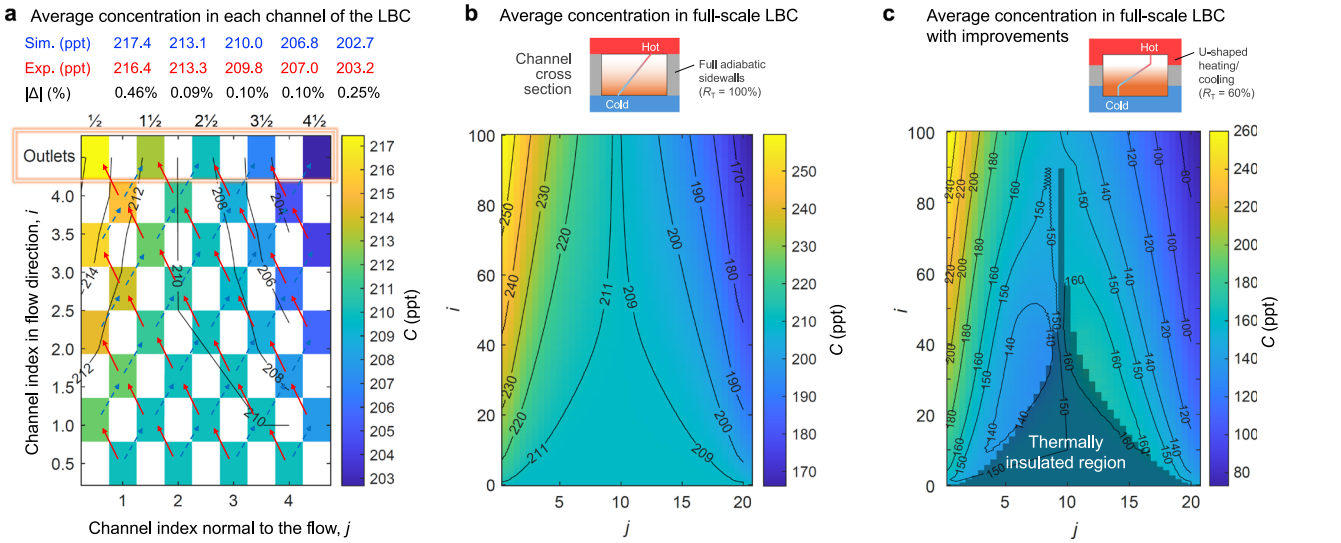

Fig. 5 | Numerical results of concentration in LBC channels. Based on simulation, the average concentration in each channel of the LBC is calculated. **a** The concentration within the lab-scale LBC at the experimental conditions: ΔT = 35 K, NaCl aqueous solution at C_0 = 210 ppt, concentration profile is fully developed in each channel (Q < 0.6 mL min^{-1}). The first row above the concentration contour plot shows the numerical results of the concentration from each outlet, while the second row is the experimental measured concentration of each outlet. The third row is the relative difference between simulation and experimental results. **b** The average concentration within a full-scale LBC with 100 × 20 channel pairs under the same experimental conditions as in **a**. A linear temperature profile was implemented in the simulation. The highest concentration within the LBC is near-saturation C > 250 ppt, while the lowest concentration is around 170 ppt. **c** The average concentration within a full-scale LBC having the same number of channels as in **b**. The linear temperature range is R_T = 60% and concentration development ratio is R_C = 0.78 for the partially developed flow. The ΔT = 35 K, seawater at C_0 = 150 ppt. The highest concentration within the LBC is near-saturation C > 250 ppt, while the lowest concentration is around 80 ppt.

In Fig. 5b, under the same temperature difference (a positive quasi-linear temperature with ΔT = 35 K) and R_C = 1 as in the lab experiment, a significant concentration change is achieved with 100 × 20 channel pairs. Our model can also calculate the important parameter SEC that measures the energy efficiency. For this work, we aim at minimising SEC without considering thermal energy recovery. More details about the energy balance and the modelling are available in the Methods section. Briefly summarising, to reduce SEC, a species developing flow configuration within each channel can be considered an operational improvement. A partially developed concentration profile means a shorter fluid residence time within each channel (as experimentally shown in Fig. 3b) but the reduction in separation should be compensated for with more channels for the same end-point concentration change. This partial separation is characterised by the concentration development ratio $R_C = \Delta C(Q)/\Delta C_{fd}$. For example, in Fig. 3b, when the concentration profile is fully developed, the volumetric flow rate is less than Q = 0.6 mL min^{-1} and ΔC_{fd} for outlet 1/2 is 6.7 ppt, while ΔC from the same outlet is 3.4 ppt for Q = 6.0 mL min^{-1}. Thus, R_C = 0.51 for Q = 6.0 mL min^{-1} while the residence time of the fluid is reduced to 10%. Note that changing R_C has a negligible effect on the heat flux. Based on our previous work (Fig. 4d of ref. 10), we identified that $R_C \approx 0.78$ increases the volumetric flow rate to 250% compared to the baseline R_C = 1. It also achieves a reduced SEC equal to about 40% of that of R_C = 1.

Importantly, a hardware-based improvement using u-shaped heating/cooling boundaries was implemented to decouple the no-flow boundary condition at the upper/lower wall boundaries from lowest/highest concentration. A linear temperature profile, as shown in the insets of Figs. 1b and 5b, results in a quasi-linear vertical concentration profile, which coincides with the zero velocity at the boundaries (due to the no-slip boundary condition). In this case, the lowest and highest concentration fluid cannot be extracted, which greatly reduces the effectiveness of the LBC. To change this unfavourable configuration, the linear temperature profile in the channel can be altered by partially changing the sidewall material, as shown in Fig. 5c inset. This can be done by etching into the metal upper and lower walls during CNC machining, or by additive manufacturing (e.g., 3D printing) of conductive materials. We previously investigated the effects of u-shaped heating and cooling on LBC performance[10]. We defined the linear temperature range R_T as the percentage of the total height of the channel that contains the linear temperature profile. When $R_T \approx 60\%$, the yield flow rate per heat rate is maximised (Fig. 5 of ref. 10), thus a minimum SEC is achieved. Figure 5c shows the concentration profile in an LBC of the same footprint area, number of channel pairs, and temperature conditions as in Fig. 5b, but under optimal parameters of R_T = 60% and $R_C \approx 0.78$ for most conditions. A much more pronounced concentration change can be achieved, around two times compared to the case without improvements in Fig. 5b, and this is accompanied by an yield flow rate increase to around 2.5 times. The SEC when the feed is seawater has been presented in Fig. 6 of ref. 10. MTD is more energy efficient under certain conditions. For desalination (Supplementary Fig. 12a[10]), the LBC is more energy efficient than other single-stage thermal desalination methods when C_0 > 100 ppt. In contrast, for brine concentration (Supplementary Fig. 12b of ref. 10), LBC is more efficient than evaporation when C_0 > 150 ppt. When considering a system at moderate high pressure of 15.51 bar (Supplementary Fig. 13[10]), SEC is significantly reduced and the MTD for brine concentration becomes more energy efficient than other single-stage thermal methods for almost any feed concentration.

Other types of concentrates

Based on literature values for the Soret coefficient and isothermal diffusion coefficients, we extended the numerical analysis to other types of concentrates that have high added values. Lithium brine (LiCl[20,21], LiI[22]), potash brine (KCl[23,24], K_2SO_4[25,26]), and sodium hydroxide (NaOH) aqueous solutions[23,27] were modelled. The channel height was 1 mm. Our modelling results show that SEC for these concentrates is comparable to or lower than those for the seawater brine. The S_T and D used for each concentrate are stated in the caption of Fig. 6 while other fluid properties, including dynamic viscosity and thermal conductivity, were those of water at 50 °C. Figure 6a–c (upper panels) shows that with increasing S_T (from left to right), the required number of channels to reach C_{yield} = 250 ppt from C_0 = 150 ppt

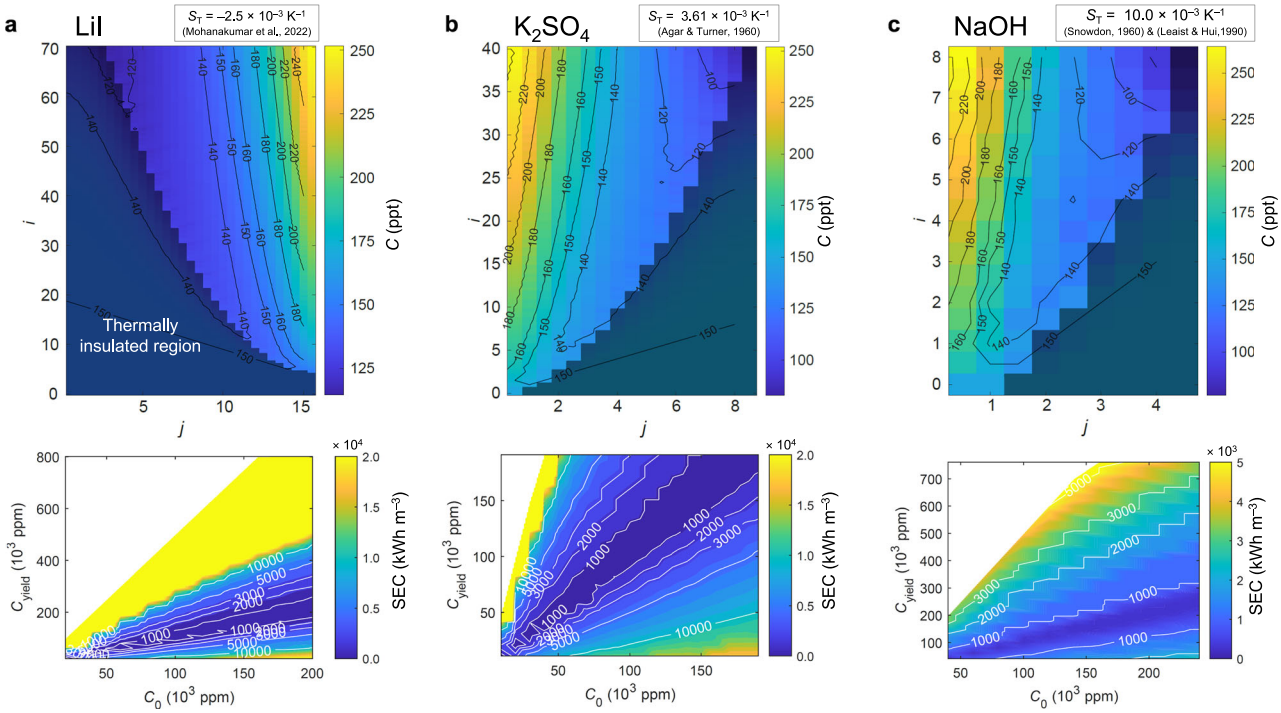

Fig. 6 | The performance of LBC for different concentrates obtained through modelling. The modelling conditions are R_T = 60%, R_C and recovery rate are selected from a parametric study to find the minimal SEC. More details on the modelling are available in the Methods section. The LBC concentration profile that increases 150 ppt to 200 ppt is shown in the upper panels. The specific energy consumption SEC (lower panels) is shown. **a** Simulation for lithium iodide (LiI) aqueous brine with properties of $S_T(25\,°C) = -2.5 \times 10^{-3}\,K^{-1}$ and $D(25\,°C) = 2 \times 10^{-9}\,m^2\,s^{-1}$, as in ref. 22. **b** Simulation for potash (K_2SO_4) aqueous brine with properties of $S_T(25\,°C) = 3.61 \times 10^{-3}\,K^{-1}$, as in ref. 26, and $D(25\,°C) = 1.35 \times 10^{-9}\,m^2\,s^{-1}$, as in ref. 25. **c** Simulation for sodium hydroxide (NaOH) aqueous concentrate with $S_T(25\,°C) = 10 \times 10^{-3}\,K^{-1}$ and $D(25\,°C) = 1.23 \times 10^{-9}\,m^2\,s^{-1}$, as in refs. 23,27. All Soret and mass diffusion coefficients are evaluated at 50 °C assuming they follow the same temperature dependence trend of the Soret and mass diffusion coefficients for aqueous NaCl[34]. The yield flow rate per channel footprint area in the LBC is 0.32, 0.34 and 0.78 $m^3m^{-2}day^{-1}$ for LiI, K_2SO_4 and NaOH, respectively.

significantly decreases. This also indicates a much higher flow rate per unit LBC channel area Q/A (excluding the footprint area where parasitic losses occur).

The analytical relationship between flow rate and the number of rows in an LBC was previously derived for fully developed concentrations under a linear vertical temperature profile, $Q \propto \frac{A}{hM}$, where A, h, and M are the footprint area, height and the number of rows of LBC, respectively (Eq. 4 in[10]). Although an analytical solution cannot be derived for temperature-dependent thermophysical properties and $R_C \neq 1$ and $R_T \neq 1$, we can model the concentration profiles in the LBC (Fig. 6a upper panels) and the corresponding SEC values as a function of feed and yield concentrations are shown in Fig. 6 lower panels. We found that due to the significantly higher S_T of the NaOH aqueous solution, the LBC-based concentration of NaOH is feasible: a significant concentration change is possible within an LBC with very few channels, similar to that of a lab-scale LBC. We note that a much larger channel area and anti-corrosion material are required. The SEC showed a relatively low value compared to the theoretical minimal SEC at 630 k W h m^{-3} for single-stage thermal evaporation without heat recovery. This is a promising future development direction for liquid separation applications based on LBC, as NaOH is a chemical, essential in many industrial processes such as the extraction of aluminium from ores[28], and is widely used around the world.

The volumetric flow rates of yield in Fig. 6 top panels were 0.32, 0.34, and 0.78 $m^3m^{-2}day^{-1}$ for LiI, K_2SO_4, and NaOH, respectively. In contrast, conventional evaporation methods, even when enhanced by optimised interfacial evaporation, typically yield much lower flow rates, approximately 0.02 $m^3\,m^{-2}\,day^{-1}$ (ref. 29) and up to 0.035 $m^3\,m^{-2}\,day^{-1}$ in more recent work[30] (assuming 8 h operation). Moreover, the modular design of our LBC system allows for vertical stacking, significantly reducing the required footprint area. This, combined with the high volumetric flow rate per unit of footprint and a comparable SEC[10], highlights the strong potential of MTD as a viable and efficient alternative to evaporation-based desalination technologies.

S_T is perhaps the most important thermophysical property that affects SEC for all conditions. S_T could also affect another important performance metric of the LBC, Q/A. This is because fewer channels are required with higher S_T to achieve a certain C_{yield}. Another important assumption that has been used in these modelling results is a perfect top–bottom flow split at the end of each channel of the LBC, i.e., the fluid flow bifurcates at the horizontal midplane into the top half and the bottom half (inset of Fig. 1b). This is called a "perfect split" as the species are separated by a horizontal midplane under a vertical temperature gradient. On the other hand, if the flow is split by a vertical midplane, no concentration difference would be achieved between the two outlet streams. The assumption of "perfect split" is valid for the lab-scale LBC prototype presented in this study due to the excellent agreement between the experimental and numerical results (Figs. 3 and 4). However, the perfect split may disappear due to scaling and fouling in the channel. Here, we define the split ratio as the concentration difference between the two streams normalised by the concentration difference when there is a perfect split (i.e., horizontal fluid flow as shown in the inset of Fig. 1b). In Fig. 7, the sensitivity analysis is performed varying S_T and the split ratio for C_0 = 150 ppt and C_{yield} = 250 ppt.

Discussion

The liquid Burgers cascade (LBC) was experimentally evaluated with a range of NaCl feed concentrations to assess its applicability to brine treatment and solute concentration for potential resource extraction. The results demonstrated the capacity of LBC to process brine with a wide range of feed concentrations, from 70 ppt (typical discharge from

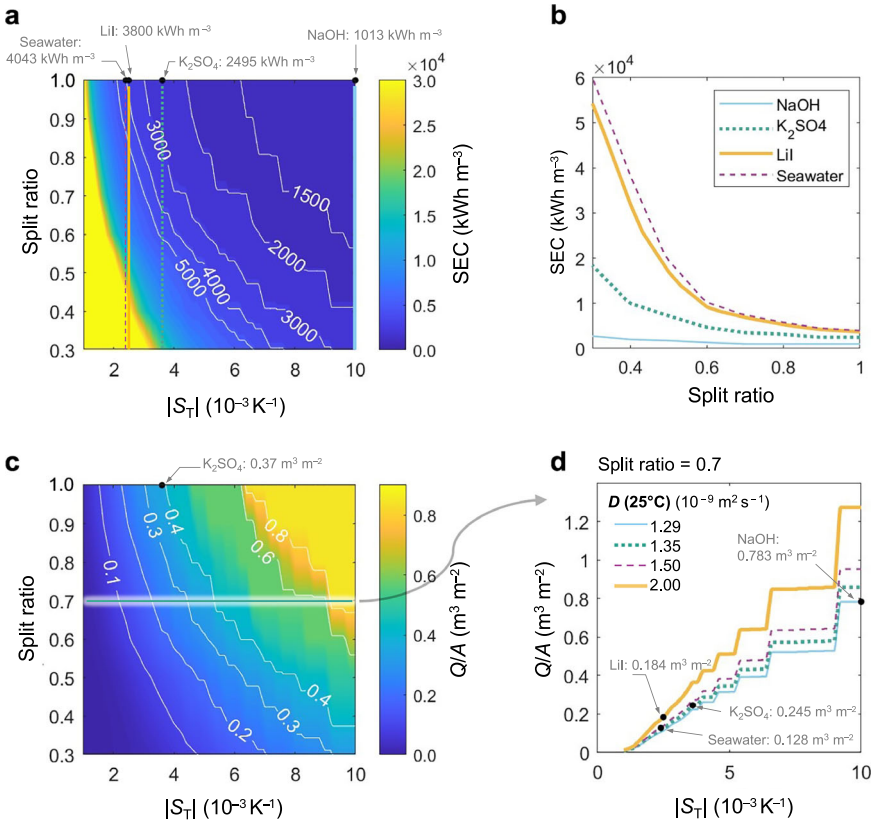

Fig. 7 | Sensitivity analysis for varying concentrating from 150 ppt to 250 ppt with LBC. **a** SEC when varying the split ratio and S_T. Split ratio is varied between 0.3 and 1 (the latter being a perfect top–bottom flow split at each channel outlet), and the absolute value of S_T is varied from 10^{-3} K^{-1} to 10×10^{-3} K^{-1}. The previous simulations assuming "perfect split" for seawater and other concentrates in Fig. 6 are labelled. The vertical lines are S_T of 2.40×10^{-3} K^{-1}, 2.50×10^{-3} K^{-1}, 3.61×10^{-3} K^{-1}, and 10.00×10^{-3} K^{-1}, corresponding to seawater brine, LiI, K_2SO_4, and NaOH aqueous solutions, respectively. **b** SEC as a function of the split ratio for four values of S_T, representing the types of feed indicated in the legend. **c** Yield flow rate per unit channel area (Q/A) per day when varying split ratio and S_T. $D(25\,°C) = 1.35 \times 10^{-9}$ m^2 s^{-1} was used, which is approximately the D of K_2SO_4. **d** Q/A is plotted for different D and split ratio is 0.7. Different concentrates are labelled.

reverse osmosis) to a hypersaline salinity of 250 ppt. Our experiments revealed that the LBC produced outlet streams with tangible salinity changes with respect to the feed concentration (exceeding 7 ppt for a relatively small LBC of 4 × 4 channel pairs), demonstrating the potential of thermodiffusive separation to concentrate or desalinate brines. The dual functionality of LBCs—concentrating brine or reducing its salinity—can support zero liquid discharge, save precious water resources in arid regions, and enable the enrichment of valuable materials such as LiI, K_2SO_4, and NaOH without reliance on large evaporation ponds or industrial evaporators. When the feed water is seawater, the SEC as a function of feed and yield concentrations was presented in our previous work[10], and an ongoing techno-economic analysis (TEA) shows that multichannel thermodiffusion (MTD) can outperform evaporation ponds for large hypersaline feed concentrations[15]. Based on the presented SEC values in Fig. 6 and the corresponding Q/A, MTD technology applied to seawater and various types of concentrates seems promising, especially when the feed has a high concentration.

While this study demonstrates the LBC performance under controlled conditions with various feed concentrations and flow rates, MTD remains a technology in early-stage development with many aspects that need further consideration in a real-environment operation. Critical factors affecting performance include scaling, imperfect stream separation, and biofouling. Initial simulations incorporating scaling effects and sensitivity analysis of flow split ratios provide insights, but long-term operational validation is essential for real-world deployment. Finally, the fabrication and testing of a 3D-printed LBC demonstrated that additive manufacturing enables rapid, low-cost prototyping while maintaining performance comparable to CNC machining. The ability to replicate geometries and explore alternative designs suggests a practical pathway for MTD as a scalable, membrane-free, chemical-free, and evaporation-free technology for the thermal treatment of brines. Addressing operational challenges and design optimisation will be crucial to establish the robustness and readiness of LBC for industrial applications.

Methods

LBC manufacturing and assembly: CNC machining

The upper and lower walls were made of aluminium (Al- Grade 6061 T651) with high thermal conductivity of 167 W m^{-1} K. The sidewalls were made of polyoxymethylene (POM) with a low thermal conductivity of 0.36 W m^{-1} K. Since subtractive machining cannot fully access the internal geometry of intertwined channels at the bifurcation points near each channel outlet, the system was split into two symmetric halves, top and bottom, each containing machined semi-channels with a depth of 1 mm. These were aligned and assembled to form the Burgers channel network[16]. For each half, a 1 mm thick POM sheet was bonded to the aluminium substrate. Aluminium and POM surfaces were prepared by sandblasting with silica abrasive at a grit size of 120 mesh (approximately 125 μm) and chemical etching to ensure strong adhesion. The channels were then machined on the POM layer. On the opposite side of the aluminium blocks, cavities were machined to serve as thermally conductive chambers for heat exchange through which hot and cold water streams are circulated (2d). A thick aluminium wall of 5 mm that separates the water bath and the brine was used, allowing rapid and uniform heat transfer. To assemble the two halves, we aligned and sealed the machined surfaces with EPDM (ethylene propylene diene monomer) O-rings around the outer perimeter of the channel area to prevent solution leakage. A two-piece high-density polyethylene (HDPE) insulation frame was added around the aluminium blocks to reduce heat loss to the ambient environment. Finally, all parts of the assembly were secured as shown in Fig. 2a using stainless steel through bolts, ensuring uniform compression, mechanical stability, and leak-free operation during experimental tests.

LBC manufacturing: 3D printing

Multichannel LBC structures were fabricated using a Prusa MK4S 3D printer. Several optimisation trials were performed to achieve the desired dimensional accuracy and surface finish across all channels. The final printing time for a high-quality structure was approximately 7 h. The LBC

was printed from thermoplastic polyurethane (TPU shore hardness 95A) through fused filament fabrication. TPU was chosen for its flexibility, water resistance, and thermal stability within the operating range of the system. 3D printing was carried out using a printing nozzle size of 0.4 mm with a layer height of 0.1 mm and a print speed of 20 mm s^{-1} to reduce the spool and improve adhesion between layers. An infill density of 85% was used to ensure high part strength and low porosity. The channel walls were 2.0 mm thick. To avoid using internal support structures that could compromise surface smoothness, aluminium inserts were waterjet-matched to the channel geometry and embedded when the print reached half of its total height. Upon completion, the metal fillers were removed. This approach produced smooth and precise internal channel surfaces, particularly in the delicate bifurcation and separation zones located at the end of each channel.

Serpentine LBC design

To investigate the impact of flow path geometry on thermodiffusive separation, a modified version of the LBC with a serpentine channel layout was developed. Instead of the standard straight configuration as originally investigated in this study, the serpentine layout (Fig. 4a) aims to reduce the perimeter of the device for a given area of footprint. The number and size of the channels were kept identical to those in the straight configuration and fabricated using the same 3D printing method and TPU filament. This configuration has smooth 180° bends at the end of a channel pair with curvature radii ranging from 6.0 mm (inner channels) to 30 mm (outer channels) to minimise flow disturbances in the bends. Since ion separation is not expected to occur in the bending regions, the upper and lower walls of these sections were made of 5.0 mm thick POM, providing thermal insulation in the bending regions. This ensures thermodiffusive separation remains confined to the straight segments. The remainder of the serpentine LBC was machined using CNC, following the same material selection and assembly method used for the straight configuration. The assembled unit was then integrated into the existing experimental setup (2a).

Experimental setup and procedure

The experiment design provides controlled volumetric flow rates, the temperature difference between the upper and lower walls of the LBC channels, and sample extraction from the LBC outlets. The system included two thermostatic water baths (cooling water bath POLYSCIENCE MXMA15R-30-A12A and heating water bath MA15H135-A12A) to set an approximate and stable temperature difference between the upper and lower walls (the exact value is measured directly with thermocouples). The hot and cold sides were set to target temperatures of 70 °C and 10 °C, respectively, generating a set vertical temperature difference of 40 K across the channels. The flow of brine through the channels was maintained using a peristaltic pump (Kamoer FX-STP2). The volumetric flow rate of the feed solution is set at a constant value of 0.6 mL min^{-1} for all tests, except for the separation sensitivity to flow rate tests, where it ranged from 0.6 mL min^{-1} to 24 mL min^{-1}. The LBC is placed horizontally and remains physically undisturbed during operation. The channels have a constant cross-sectional area, even at the channel bifurcation.

Brine solutions with target concentrations were prepared using laboratory-grade NaCl (measured with the Shimadzu ATX224 analytical balance) dissolved in deionised water. The feed solution was stored in an elevated reservoir relative to the LBC unit, as shown in Fig. 2d, e, enabling gravity-assisted feeding and avoiding air bubbles. A degassing unit is also placed on the feed line to eliminate air bubbles before entering the LBC. The inlet was positioned slightly below the lower channel walls to ensure proper filling, while the five outlets were located at the top of the channels on the opposite side of the unit. These outlets directed the flow into five dedicated collection bottles. Each experiment began with a startup phase lasting approximately 1.5 h to 2 h, during which the system reached steady-state thermal and concentration conditions; any water collected during this phase was discarded. Following stabilisation, the main collection phase commenced and the experiment was continuously monitored for approximately 5 h until all collected yield in the bottles exceeded 40 mL for the three outlets (1+1/2, 2+1/2 and 3+1/2) and 20 mL for the edge outlets (1/2 and 4+1/2). After each experiment, to eliminate the risk of contamination for the next day's experiment, the LBC channels were flushed with deionised water and then dried with air flow.

Measurement of concentration difference

For binary NaCl/H_2O solution, accurate digital interferometry with a temporal phase-shifting technique and a rotating polariser, as described in ref. 18, was used to visualise the transient concentration difference between two solutions extracted from the LBC experiment. A shearing cell experiment (Supplementary Fig. 3 of ref. 10) was used to create a diffusion field between high- and low-concentration solutions. The bottom half of the cell was fixed and filled with the high-concentration solution, while the top half was filled with the low-concentration solution before it was slid on top of the high-concentration solution. Then a one-dimensional diffusion field was triggered between the low- and high-concentration solutions and visualised with phase-shifting interferometry (PSI), similar to ref. 31. From PSI images, the unwrapped phase difference $\Delta\psi$ can be obtained, and it is directly related to ΔC by

$$\Delta C = \frac{\Delta\psi}{\mathrm{OP\,CF}}, \tag{2}$$

where the contrast factor CF describes the relationship between $\Delta\psi$ and ΔC, and OP is the optical path. The CF was experimentally measured based on three replicates. $\Delta\psi$ ranges between 0 and $2N\pi$, where N is the number of fringes observed in the phase-shifted data. The typical relative measurement error ($\delta\Delta C/\Delta C$) based on PSI and the shearing cell method is less than 10%. This was calculated by error propagation considering the errors in CF and $\Delta\psi$. OP is a fixed value as the optical setup and the shearing cell were the same in all measurements. The relative error $\delta\Delta C/\Delta C$ is thus

$$\frac{\delta\Delta C}{\Delta C} = \left[\left(\frac{\delta\Delta\psi}{\Delta\psi}\right)^2 + \left(\frac{\delta \mathrm{CF}}{\mathrm{CF}}\right)^2\right]^{0.5}. \tag{3}$$

The error in the unwrapped phase difference, $\delta\Delta\psi$, is the standard deviation when $\Delta\psi$ is obtained for each phase-shifted data. Approximately 50 phase-shifted data were taken for each measurement to reduce uncertainty. The typical value of $\delta\Delta\psi$ was 3.4%. The relative error $\frac{\delta \mathrm{CF}}{\mathrm{CF}}$ was 5.4% ($0.56 \pm 0.03\pi$ g mg^{-1} mm) for the PSI using the shearing cell method. Thus, the propagated error for $\frac{\delta\Delta C}{\Delta C}$ was approximately 10%.

Energy consumption of the liquid Burgers cascade

SEC is an essential performance metric for any water treatment method, particularly because desalination or brine concentration are generally considered energy-intensive processes. Here, the calculation of SEC of the LBC is presented. We consider only the energy flow in the LBC and the energy equation can be expressed as:

$$\frac{D}{Dt}\int_{\mathrm{sys}} e\rho\,\mathrm{d}\forall = \left(\sum \dot{Q} + \sum \dot{W}\right)_{\mathrm{sys}}. \tag{4}$$

Here, the time rate of increase of the total stored energy of the system is equivalent to the rate of net heat transfer $\dot{Q}$ and work transfer $\dot{W}$ into the system, and e is the stored energy per unit mass. For a simplified assumption where the flow velocity is constant and there is no height difference between the inlet and the outlet of the channel, the stored energy can be simplified to be the internal energy so that $e = \breve{u}$ and the left-hand side of the equation can be simplified. Here, the change in internal energy is due to two factors: the change in temperature and the change in salinity. That is $\breve{u} = \breve{u}_T + \breve{u}_C$. $\breve{u}_C$ is the energy gain due to the created salinity gradient and can be calculated in the same way as the well-known thermodynamic limit for desalination (i.e., theoretical minimum energy of separation) based on the Gibbs free energy for separation[32]. For desalination of seawater, $\breve{u}_C$ is around

1 kWh tonne^{-1}. However, $\breve{u}_C$ is dependent on the concentration of feed water and yield, as well as the recovery rate R_w of the separation process. The minimal SEC of produced water $\breve{u}_C$ can be calculated as:

$$\breve{u}_C = 2\frac{RT}{\rho}\left[\frac{c_f}{R_w}\ln\frac{c_b}{c_f} - c_y \ln\frac{c_b}{c_y}\right], \tag{5}$$

where c is the molar concentration and subscript f, y, b denotes feed, yield and the brine discharge, respectively. R is the gas constant and T is the absolute temperature. When c_f and c_y are known, then $c_b = \frac{c_f - R_w c_y}{1-R_w}$ based on mass conservation. The above equation can be further simplified:

$$\breve{u}_C = 2\frac{RT}{\rho}\left[\frac{c_f}{R_w}\ln\frac{c_f - R_w c_y}{c_f(1-R_w)} - c_y \ln\frac{c_f - R_w c_y}{c_y(1-R_w)}\right]. \tag{6}$$

$\breve{u}_C$ is less than 20 kWh tonne^{-1}.

Now we consider $\breve{u}_T$ due to the change in temperature. For incompressible flow,

$$\breve{u}_T = \frac{1}{h}\int_0^h c_p(T(y) - T_f)dy, \tag{7}$$

where c_p is the specific heat capacity at constant pressure and $\breve{u}_T \approx 40$ kWh tonne^{-1}.

The work rate $\dot{W}$ is only related to the fluid pressure P acting on the control surface, and in the case of the LBC:

$$\dot{W} = \int_{cs} -P\mathbf{u}\hat{n}\ \mathrm{d}A_{cs} = Q(-P_{in} + P_{out}), \tag{8}$$

where A_{cs} is the control surface area normal to the flow direction and Q is the volumetric flow rate. Therefore, the only electrical energy input into the TSU channel is related to the operation of the pumps to overcome the pressure drop. For a rectangular channel, the pressure drop ΔP can be calculated as:

$$\Delta P = f\frac{l}{D_h}\frac{\rho V^2}{2}, \tag{9}$$

where f is the friction factor that can be calculated based on the aspect ratio w/h of the individual channel; lowercase l, w, h denotes the length, width, and height of the channel, respectively. The hydrodynamic diameter D_h is calculated as $D_h = \frac{2wh}{w+h}$.

To verify the pressure drop analytical solution, we compare it with a high-fidelity CFD that was performed for the gas Burgers cascade in the literature[33]. The pressure drop through the gas Burgers cascade is 7.9 Pa as reported in ref. 33. The total pressure drop can be calculated as $\Delta P \times 2M \times N$ when ignoring the impedance imposed by the bifurcation and recombination structure at the ends of each channel, and we obtain a total pressure drop of 6.5 Pa for the CO_2/H_2 gas Burgers cascade. Therefore, the analytical solution provides a good approximation for the pressure drop in the Burgers cascade. The pressure drop is always less than 1 bar for a reasonable large LBC (Supplementary Fig. 13 of ref. 12).

Starting with an individual channel, $\dot{Q}_{in}$ is the heat rate that sustains the temperature gradient across the channel height. $\dot{Q}_{in}$ can be approximated with the one-dimensional Fourier's law for heat conduction.

$$\dot{Q}_{in} = kA\frac{\Delta T}{hR_T}, \tag{10}$$

where R_T is the ratio of the height with a linear temperature gradient. A is the lateral area of the LBC. Now the energy balance of the LBC, Eq. (4), can be rearranged with the energy inputs on the left-hand side:

$$\dot{Q}_{in} + \dot{W} = Q\rho(\breve{u}_C + \breve{u}_T) + \dot{Q}_{out}. \tag{11}$$

Note here Q is the volumetric flow rate, while $\dot{Q}$ is the heat rate. This is shown by the Sankey diagram in Fig. 2c. The SEC is calculated considering only $\dot{Q}_{in}$:

$$\mathrm{SEC} = \frac{\dot{Q}_{in}}{Q}. \tag{12}$$

We see that SEC is based on idealised conduction modelling without considering parasitic losses of heat to the environment. For the lab-scale LBC, approximately 50% of heat is transferred through the water due to an unnecessarily large sidewall structure (see Methods of ref. 10). That is, under realistic conditions, the actual SEC could be twice as large as reported. However, it is also important to note that we did not consider any heat recovery for $\dot{Q}_{in}$, which could lead to significant reduction in SEC as well, nor improved designs with reduced sidewall structure.

Liquid Burgers cascade modelling

Our in-house MATLAB code (version 8c), which is open source[19], can calculate the specific energy consumption (SEC) and the volumetric flow rate of the yield per unit area ($\frac{Q}{A}$) of a full-scale LBC based on user input. The first step requires the user to determine the input parameters, including temperature difference (ΔT), mean temperature (T_{mean}), Soret and mass diffusion coefficients at room temperature (S_T(25 °C)), D(25 °C), and feed concentration C_0. Importantly, a potential type of degradation is due to scaling, the accumulation of solids on the channel walls, and acts as an additional thermal barrier that reduces the effective temperature difference in the liquid phase, ΔT_f. The effect of scaling on ΔT_f can be evaluated with a one-dimensional thermal resistance network that includes scales on both the upper and lower walls of the channel and considers the temperature difference in the scales and liquid. The heat flux through the scales and liquid is:

$$q = \frac{\Delta T_f}{R_f} = \frac{\Delta T_s}{R_s}, \tag{13}$$

where ΔT_s is the temperature difference in the scales. The thermal resistance of the scales on each side is $R_s = t_s/k_s$, where t_s and k_s are the thickness and thermal conductivity of the solid scales, respectively. The thermal resistance of the liquid when the flow speed is relatively low can be approximated by $R_s = (h - 2t_s)/k_f$, where h is the height of the channel and k_f is the thermal conductivity of the fluid.

$$\Delta T = 2\Delta T_s + \Delta T_f \tag{14}$$

We can then derive the following ratio.

$$\frac{\Delta T_f}{\Delta T} = \frac{k_s(h - 2t_s)}{k_s h - 2k_s t_s + 2k_f t_s} \tag{15}$$

This ratio is a code input that ensures the target C_{yield} is still achieved even when scaling occurs. Moreover, when the scaling is not as severe as in the modelled LBC case, the feed can pass through the LBC faster (reduced R_C) so that the same C_{yield} is achieved, but with a higher Q/A.

The changes in S_T and D reflect different species. The code can also vary the split ratio that indicates how perfect the flow bifurcation is at the end of each channel (Fig. 1b and Supplementary Fig. 6 of ref. 10). The split ratio accounts for flow dynamics, scaling, and fouling.

A range is first defined for feed and yield concentrations ranges, C_0 and C_{yield}, through which the code iterates. From the second step forward, all calculations are captured by the in-house code, and no further user input is required. In the second step, the code calculates the concentration difference

between boundaries, $\Delta C_{0,\mathrm{wall}}$. The mass flux **J** under thermodiffusion is given by Eq. (1). Thus in steady state when $\mathbf{J} = 0$, $\Delta C_{0,\mathrm{wall}}$ can be approximately to be $\Delta C_{0,\mathrm{wall}} = S_T(T_{\mathrm{mean}})\Delta T C(1 - C)$, when a linear temperature profile is considered. Also, τ, the time for concentration profile to fully develop, can be calculated as:

$$\tau = \frac{h^2}{\pi^2 D(T_{\mathrm{mean}})}. \tag{16}$$

Both S_T and D are assumed to follow the same temperature dependency of that of NaCl/H_2O[34] so that $S_T(T_{\mathrm{mean}})$ and $D(T_{\mathrm{mean}})$ can be calculated.

In the third step, two lookup tables are produced, one for the developing concentration profile (R_C) and another for the non-linear vertical temperature profile (R_T) created by the u-shaped conductive boundaries. Previously, based the characteristic of the transient concentration behaviour, in which the separation first develops quickly and then gradually approaches steady state (Fig. 4c of ref. 10), we see that partial separation in a concentration developing flow can allow for higher flow rates even when achieving the same concentration drop with more channels (Fig. 4d of ref. 10). To include the effect of a developing concentration profile, the first lookup table between $R_C = \Delta C_{0,\mathrm{wall}}(t)/\Delta C_{0,\mathrm{wall}}(\tau)$ and t/τ is produced. R_C has little impact on $\dot{Q}_{\mathrm{in}}$ but affects SEC via Q as in Eq. (12). The non-linear temperature profile improves separation by decoupling the lowest or highest concentration from the zero-velocity at the top and bottom boundaries (Fig. 5a of ref. 10). For a linear C profile and a parabolic velocity profile, concentration difference between the top steam and the bottom stream ΔC_0 is $\frac{\Delta C_{0,\mathrm{wall}}}{4.32}$ (Supplementary Fig. 14a of ref. 10). Based on the R_T lookup table (Fig. 5b of ref. 10), we now obtain $\Delta C_0'$, which is larger than ΔC_0. We noticed that symmetric $R_T = 60\%$ results in the lowest SEC for different R_C (Fig. 5c of ref. 10). Thus $R_T = 60\%$ is used. However, it is worth noting that when using non-linear temperature profile assumption, the channel cross section has to have an aspect ratio (width/height) below 0.5 (Supplementary Fig. 4 of ref. 10). For each combination of $C_0 \rightarrow C_{\mathrm{yield}}$ a parametric study of recovery rate R_W and R_C is performed. All combinations of R_W between 20% and 80% with a step of 5% and R_C between 0.5 and 1 with a step of 0.1 are examined to find the minimal SEC. For desalination, the optimal R_W is typically in the range of 50–60%, while the optimal R_W for brine concentration is typically of 20–30% (Supplementary Fig. 9 of ref. 10).

Now in the fourth step, we begin mapping the concentration in all channels within the LBC to meet the desired C_{yield}, starting with a certain C_0. Based on Eq. (1), when the feed concentration at the channel inlet is $C_{i,j}$, $\Delta C_{i,j} \approx \Delta C_0' \frac{C_{i,j}(1-C_{i,j})}{C_0(1-C_0)}$. Separation can be determined without calculating or modelling the concentration profile in each channel. For the first row where $i = 0.5$, $C_{0.5,j} = C_0$. Then we propagate the concentration in the direction of fluid flow. For any $i = n$, the concentrations in the two half-channels on the edges are $C_{n,1/2} = C_{n-1/2,1} + \Delta C_{n-1/2,1}$, $C_{n,N+1/2} = C_{n-1/2,N} - \Delta C_{n-1/2,N}$ and for all channels in the middle, $C_{n,j} = [(C_{n-1/2,j-1/2} - \Delta C_{n-1/2,j-1/2}) + (C_{n-1/2,j+1/2} + \Delta C_{n-1/2,j+1/2})]/2$. When $i = n + 1/2$, for the two full channels at the edges, $C_{n+1/2,1} = [C_{n,0.5} + (C_{n,1+1/2} + \Delta C_{n,1+1/2})]/2$ and $C_{n+1/2,N} = [(C_{n,N-1/2} - \Delta C_{n,N-1/2}) + C_{n,N+1/2}]/2$, and for all channels in the middle, $C_{n+1/2,j} = [(C_{n,j-1/2} - \Delta C_{n,j-1/2}) + (C_{n,j+1/2} + \Delta C_{n,j+1/2})]/2$. This calculation continues until $i = M$, and the concentration is calculated in all LBC channels.

In the fourth step, the number of rows (M) and columns (N) are optimised so that the flow rate is maximised while satisfying the concentration drop requirement. In our previous work (Eq. 4 of ref. 10), we found that when the operating conditions are kept unchanged (including C_0, ΔT, T_{mean}, S_T, D, R_C, and R_T), minimising M will improve energy efficiency:

$$\frac{Q}{A} \propto \frac{1}{hM}, \qquad \mathrm{SEC} \propto M^{-1}. \tag{17}$$

In the fifth and last step, SEC and Q/A are output as two separate contour plots for a range of C_0 and C_{yield}, which is reported in this article.

Data availability

Source data are available through Figshare at https://doi.org/10.6084/m9.figshare.29421782 (ref. 35). All other data supporting the findings of this study are available from the corresponding author upon reasonable request. The code for thermodiffusive separation in multichannel devices developed for this study is available on GitHub[36].

Received: 4 July 2025; Accepted: 9 October 2025;
Published online: 18 November 2025

References

1. Panagopoulos, A. & Haralambous, K.-J. Environmental impacts of desalination and brine treatment-challenges and mitigation measures. *Mar. Pollut. Bull.* **161**, 111773 (2020).
2. Sirota, R. et al. Impacts of desalination brine discharge on benthic ecosystems. *Environ. Sci. Technol.* **58**, 5631–5645 (2024).
3. Ihsanullah, I. et al. Waste to wealth: A critical analysis of resource recovery from desalination brine. *Desalination* **543**, 116093 (2022).
4. Roberts, J. et al. Desalination brine disposal methods and treatment technologies – a review. *Sci. Total Environ.* **650**, 1258–1270 (2018).
5. Scelfo, G. et al. Demonstration of ultra-high-water recovery and brine concentration in a prototype evaporation unit. *Sep. Purif. Technol.* **354**, 129427 (2025).
6. Guo, J., Tucker, Z. D., Wang, Y., Ashfeld, B. L. & Luo, T. Ionic liquid enables highly efficient low temperature desalination by directional solvent extraction. *Nat. Commun.* **12**, 437 (2021).
7. Vera, M. L., Torres, W. R., Galli, C. I., Chagnes, A. & Flexer, V. Environmental impact of direct lithium extraction from brines. *Nat. Rev. Earth Environ.* **4**, 149–165 (2023).
8. Jena, S. K. A review on potash recovery from different rock and mineral sources. *Min., Metall. Explor.* **38**, 47–68 (2021).
9. Amoatey, P. et al. A critical review of environmental and public health impacts from the activities of evaporation ponds. *Sci. Total Environ.* **796**, 149065 (2021).
10. Xu, S. & Torres, J. F. All-liquid thermal desalination and brine concentration via multichannel thermodiffusion. *Nat. Water* **3**, 617–631 (2025).
11. Platten, J. K. The soret effect: a review of recent experimental results **73**, 5–15 (2006).
12. Xu, S., Hutchinson, A. J., Taheri, M., Corry, B. & Torres, J. F. Thermodiffusive desalination. *Nat. Commun.* **15**, 2996 (2024).
13. Torres, J. F., Komiya, A., Henry, D. & Maruyama, S. Measurement of soret and fickian diffusion coefficients by orthogonal phase-shifting interferometry and its application to protein aqueous solutions. *J. Chem. Phys.* **139**, 074203 (2013).
14. Cussler, E. L. *Diffusion: Mass transfer in fluid systems* (Cambridge University Press, 2009).
15. Jackson, C., Xu, S. & Torres, J. F. Techno-economic analysis of multichannel thermodiffusion for desalination and brine concentration. *npj Clean Water* https://doi.org/10.21203/rs.3.rs-7164135/v1 (2025). (In press).
16. Watanabe, S., Matsumoto, S., Higurashi, T., Yoshikawa, Y. & Ono, N. Almost complete separation of a fluid component from a mixture using burgers networks of microseparators. *J. Phys. Soc. Jpn.* **84**, 043401 (2015).
17. Xu, S., Komiya, A., Corry, B. & Torres, J. F. Scaling up thermodiffusive separation through a microchannel. *Proceedings of the 23rd Australasian Fluid Mechanics Conference* 438 (2022).
18. Torres, J. F., Komiya, A., Shoji, E., Okajima, J. & Maruyama, S. Development of phase-shifting interferometry for measurement of isothermal diffusion coefficients in binary solutions. *Opt. Lasers Eng.* **50**, 1287–1296 (2012).
19. Xu, S. In-house code for designing liquid Burgers cascade https://github.com/Sahauaqa/LBC_Performance.git (2024).

20. Colombani, J., Bert, J. & Dupuy-Philon, J. Thermal diffusion in (LiCl, RH_2O). *J. Chem. Phys.* **110**, 8622–8627 (1999).
21. Lee, N., Mohanakumar, S., Wiegand, S. & Briels, W. J. Non-monotonic Soret coefficients of aqueous LiCl solutions with varying concentrations. *Phys. Chem. Chem. Phys.* **26**, 7830–7836 (2024).
22. Mohanakumar, S., Kriegs, H., Briels, W. & Wiegand, S. Overlapping hydration shells in salt solutions causing non-monotonic Soret coefficients with varying concentration. *Phys. Chem. Chem. Phys.* **1077**, 27380–27387 (2022).
23. Snowdon, P. N. & Turner, J. C. R. The Soret effect in some 0.01 normal aqueous electrolytes. *Trans. Faraday Soc.* **56**, 1409–1418 (1960).
24. Römer, F., Wang, Z., Wiegand, S. & Bresme, F. Alkali halide solutions under thermal gradients: Soret coefficients and heat transfer mechanisms. *J. Phys. Chem. B* **117**, 8209–8222 (2013).
25. Mullin, J. W. & Nienow, A. W. Diffusion coefficients of potassium sulfate in water: diffusivity heat of formation of trinitrochloromethane by combustion calorimetry. *J. Chem. Eng. Data* **94**, 526–527 (1964).
26. Agar, J. N. & Turner, J. C. R. Thermal diffusion in solutions of electrolytes. *Proc. R. Soc. A: Math., Phys. Eng. Sci.* **255**, 307–330 (1960).
27. Leaist, D. G. & Hui, L. Conductometric determination of the soret coefficients of a ternary mixed electrolyte. Reversed thermal diffusion of sodium chloride in aqueous sodium hydroxide solutions. *J. Phys. Chem.* **94**, 447–451 (1990).
28. Adamson, A. N., Bloore, E. J. & Carr, A. R. *Basic Principles of Bayer Process Design* (Springer International Publishing, 2016).
29. Ni, G. et al. A salt-rejecting floating solar still for low-cost desalination. *Energy Environ. Sci.* **11**, 1510–1519 (2018).
30. Mohsenzadeh, M., Aye, L. & Christopher, P. Development and experimental analysis of an innovative self-cleaning low vacuum hemispherical floating solar still for low-cost desalination. *Energy Convers. Manag.* **251**, 114902 (2022).
31. Guo, Z., Maruyama, S. & Komiya, A. Rapid yet accurate measurement of mass diffusion coefficients by phase shifting interferometer. *J. Phys. D: Appl. Phys.* **32**, 995 (1999).
32. Wang, L., Violet, C., Duchanois, R. M. & Elimelech, M. Derivation of the theoretical minimum energy of separation of desalination processes. *J. Chem. Educ.* **97**, 4361–4369 (2020).
33. Kyoda, T., Saiki, T., Matsumoto, S., Watanabe, S. & Ono, N. Performance improvement of a micro-structured gas separator utilizing the Soret effect. *J. Therm. Sci. Technol.* **17**, 1–15 (2022).
34. Caldwell, D. R. Thermal and Fickian diffusion of sodium chloride in a solution of oceanic concentration. *Deep-Sea Res. Oceanogr. Abstr.* **20**, 1029–1039 (1973).
35. Mohsenzadeh, M., Xu, S., Shamet, O. & Torres, J. F. Figshare dataset for article scalable brine treatment using 3D-printed multichannel thermodiffusion. *Figshare* https://doi.org/10.6084/m9.figshare.29421782 (2025).
36. Xu, S. In-house code for designing liquid burgers cascade. *GitHub repository* https://github.com/Sahauaqa/LBC_Performance.git (2025).

Acknowledgements

This research was funded by the Australian Department of Foreign Affairs and Trade (Grant type: SciTech4Climate) and Wacomet Water Co. The authors thank Mr Junxiang Zhang for designing and manufacturing the shearing cell for phase-shifting interferometry measurements. The authors thank Dr Mona E. Mahani from the ANU Institute for Climate, Energy and Disaster Solutions for the continued support and advice. We express our sincere gratitude to Aaron Mandell from Wacomet Water Co. for his generous philanthropic donation that enabled this work.

Author contributions

J.F.T. conceived the idea of the liquid Burgers cascade (LBC), acquired funding, supervised the co-authors, managed the project, co-designed the LBC and experiments, and wrote the Introduction. M.M. co-designed the LBC and experiments, built the LBC, performed LBC experiments, and wrote the experimental sections. S.X. co-designed the LBC and experiments, developed the LBC experimental procedure, performed PSI characterisation of LBC samples, coded the multichannel device model, ran full-scale separation and energy consumption simulations, wrote the modelling sections, and analysed experimental data. O.S. performed LBC experiments and PSI characterisation of LBC samples, and analysed experimental data. All authors reviewed and approved the manuscript.

Competing interests

J.F.T. and S.X. declare a financial competing interest. They filed an international patent application (No. PCT/AU2025/051021) on the multichannel water treatment device described in the article. J.F.T and S.X. are both affiliated with and hold ownership in Soret Technologies Pty Ltd, which may benefit from the publication of this research. M.M. and O.S. declare no competing interests.

Additional information

Correspondence and requests for materials should be addressed to Juan F. Torres.